

Transmission property of one-dimensional Dirac-semimetal-defected photonic crystal in terahertz multi-bandgap

Ji-Kai Wang(王济凯), Li Jiang(姜丽), Xue-Fei Yang(杨雪菲), and Ji-He Zhao(赵继和)
Citation: Chin. Phys. B, 2026, 35 (**1**): 014209. DOI: 10.1088/1674-1056/ade4b3
http://cpb.iphy.ac.cn; http://iopscience.iop.org/cpb

What follows is a list of articles you may be interested in

Giant-tunable bidirectional Goos-Hänchen shifts via phase change material-based metasurfaces with quasi-bound states in continuum

Jiaqing Liu(刘佳晴), Yue Zheng(郑悦), Xiao Li(李潇), Jingwen Li(李静文), Guohao Zhang(张国昊), Daxing Dong(董大兴), Dongmei Liu(刘冬梅), Yuwen Jia(贾玉雯), Yangyang Fu(伏洋洋), and Youwen Liu(刘友文)
Chin. Phys. B, 2025, 34 (**7**): 074208. DOI: 10.1088/1674-1056/adcdee

Reconfigurable microring resonators for multipurpose quantum light sources

Yuxing Du(杜昱星), Yingwen Liu(刘英文), Chao Wu(吴超), Pingyu Zhu(朱枰谕), Chang Zhao(赵畅), Miaomiao Yu(余苗苗), Yan Wang(王焱), Kaikai Zhang(张凯凯), and Ping Xu(徐平)
Chin. Phys. B, 2025, 34 (**7**): 074207. DOI: 10.1088/1674-1056/adcc88

Controllable optical bistability in a Fabry-Pérot cavity with a nonlinear three-dimensional Dirac semimetal

Hong-Xia Yuan(袁红霞), Jia-Xue Li(李佳雪), Qi-Jun Ma(马奇军), Hai-Shan Tian(田海山),Yun-Yang Ye(叶云洋), Wen-Xin Luo(罗文昕), Xing-Hua Wu(吴杏华), and Le-Yong Jiang(蒋乐勇)
Chin. Phys. B, 2024, 33 (**3**): 034213. DOI: 10.1088/1674-1056/acfdfe

Enhanced and controllable reflected group delay based on Tamm surface plasmons with Dirac semimetals

Qiwen Zheng(郑棋文), Wenguang Lu(卢文广), Jiaqing Xu(胥加青),Yunyang Ye(叶云洋), Xinmin Zhao(赵新民), and Leyong Jiang(蒋乐勇)
Chin. Phys. B, 2023, 32 (**7**): 074208. DOI: 10.1088/1674-1056/aca205

Thermal tunable one-dimensional photonic crystals containing phase change material

Yuanlin Jia(贾渊琳), Peiwen Ren(任佩雯), and Chunzhen Fan(范春珍)†
Chin. Phys. B, 2020, 29 (**10**): 104210. DOI: 10.1088/1674-1056/abab78

Transmission property of one-dimensional Dirac-semimetal-defected photonic crystal in terahertz multi-bandgap

Ji-Kai Wang(王济凯), Li Jiang(姜丽)†, Xue-Fei Yang(杨雪菲), and Ji-He Zhao(赵继和)

Changchun University of Science and Technology, Changchun 130000, *China*

(Received 15 April 2025; revised manuscript received 26 May 2025; accepted manuscript online 16 June 2025)

A symmetrical one-dimensional (1D) photonic crystal structure with a Dirac-emimetal-defected layer is proposed. The material properties of the Dirac semimetal are governed by three key parameters: Fermi level, Fermi velocity, and degeneracy factor. Simulation results demonstrate that the proposed structure generates multiple photonic bandgaps within the THz frequency range. In the low-THz region, pronounced resonant transmission peaks emerge, enabling near-perfect filtering performance. The positions of these defect modes can be dynamically tuned by adjusting the Fermi level and degeneracy factor. In mid- and high-THz frequency bands, the Dirac semimetal begins to exhibit metallic behavior, leading to attenuation of the transmission peaks and the appearance of absorption. The elevation of the Fermi level delays the critical threshold for the transition from the dielectric state to the metallic state, while an increase in Fermi velocity suppresses metallic behavior. Therefore, enhancing both the Fermi level and Fermi velocity contributes to strengthening the defect peak intensity. Conversely, increasing the degeneracy factor strengthens the metallic characteristics, thereby disrupting the high-frequency photonic bandgap. Notably, the defect layer thickness and incident angle exert significant influence on the transmission behavior: a larger incident angle causes the defect peak to shift toward higher frequencies and reduces its intensity, whereas a thicker defect layer shifts the defect peak toward lower frequencies. The modulation effects of both parameters become more pronounced as frequency increases. Compared with conventional photonic crystals, our work can provide a tunable structure over transmission properties, offering novel strategies for designing tunable filters and optical sensors.

Keywords: one-dimensional photonic crystal, Dirac semimetal, tunability, THz

PACS: 42.70.Qs, 42.25.Bs, 78.67.Pt

DOI: 10.1088/1674-1056/ade4b3 **CSTR:** 32038.14.CPB.ade4b3

1. Introduction

THz waves lie between microwaves and infrared waves. While microwaves and infrared waves have been extensively studied, research on THz remains relatively limited. Since THz is in the direction of transition from macroscopic electronics to microscopic photonics, this particular existence also leads to the emergence of unique properties (high transmittance, low-energy, transient, *etc*.) and a wide range of applications for THz.[1–4] However, the weak interaction between natural materials and THz radiation poses significant challenges in the development of functional THz devices.

Photonic crystals are artificial periodic structures composed of two or more materials with different dielectric constants. Due to their unique electromagnetic properties and potential applications, they have attracted significant research interest.[5,6] Just as the principle of electronic bandgap the semiconductor, there exists the photonic bandgap in the photonic crystals, in which electromagnetic waves cannot propagate within a specific frequency range. The phenomenon arises from the Bragg scattering interference effect in periodic dielectric structures.[7] In 1D photonic crystals, an omnidirectional photonic bandgap can be achieved, preventing electromagnetic waves from propagating at any angle of incidence and polarization state. This property holds great potential for applications in highly reflective mirror structures,[8,9] omnidirectional optical fibers,[10,11] and other photonic devices. Conventional photonic crystals are typically composed of graphene, metals, or semiconductor materials. The strong light absorption properties of metals make them ideal candidates for photonic crystal absorber design.[12] Graphene, due to its high electron mobility and low absorption of electromagnetic waves,[13] is commonly used in composite structures for multichannel optical filtering and visible light absorption.[14,15] However, the high ohmic losses in metals, combined with the inherent losses and limited tunability of graphene, restrict their effectiveness in photonic crystal bandgap modulation.

Similar to those of graphene, Dirac semimetal (DS) exhibits remarkable electrical properties, including their exceptional conductivity, high electron mobility, and unique energy band structure. In addition, the Dirac semimetal exhibits remarkable electrical properties, including high magnetoresistance and ultrahigh carrier mobility, making them highly

†Corresponding author. E-mail: jiangli@cust.edu.cn

© 2026 Chinese Physical Society and IOP Publishing Ltd. All rights, including for text and data mining, AI training, and similar technologies, are reserved.

promising for applications in tunable photonic devices and next-generation electronic devices.[16–19] As a dielectric material for photonic crystals, the conductivity of DS varies with the Fermi level, while their dielectric function can also be tuned via electrostatic gating. Compared to graphene, DS possesses higher carrier mobility and exhibits linear frequency-dependent absorption characteristics.[20,21] Moreover, the DS materials exhibit a high nonlinear refractive index, effectively reducing plasma losses in the THz regime. Due to the crystal symmetry protection in Dirac semimetal, which prevents the formation of a bandgap, their nonlinear optical properties are superior to those of conventional metallic materials.[22]

In recent years, the theoretical predictions and experimental demonstrations of bulk DS, such as Na_3Bi, $ZrTe_5$, and Cd_3As_2, have garnered significant interest.[23–26] The unique properties of DS make them ideal candidates for integration into nonlinear photonic and optoelectronic devices. Zhao *et al.*[27] theoretically investigated the tunability of the omnidirectional bandgap (OBG) of a 1D photonic crystal composed of a DS and an SiO_2 dielectric by adjusting the structural Fermi level. Wang *et al.*[28] studied the transmission characteristics of 1D photonic crystals containing dielectric materials and DS, revealing the existence of tunable defect modes. You *et al.*[29] theoretically explored the absorption characteristics of 1D periodic structures composed of alternating three-dimensional (3D) DS layers and dielectric layers. Wang *et al.*[30] proposed a tunable bifunctional THz metamaterial device based on a DS thin film and VO_2, capable of achieving tunable broadband asymmetric transmission of linearly polarized THz waves. Meng *et al.*[31] introduced a novel bidirectional tunable THz perfect absorber based on a DS Al-CuFe quasicrystal structure, which achieves near-perfect absorption regardless of whether the incident light is from the front or back of the system. Wang *et al.*[32] developed a hybrid photodetector based on the topological DS $PtSe_2$, designed for efficient low-energy photon harvesting. By optimizing the antenna structures, Ohmic contacts, van der Waals heterojunctions, and absorption structures, the device performance was significantly enhanced. Experimental results also demonstrated the potential of this device for lossless THz imaging. Li *et al.*[33] proposed a THz narrowband perfect absorber based on a DS–graphene composite structure, achieving near-100% absorption efficiency. By adjusting the conductivity of graphene, the position and intensity of the absorption peak could be dynamically controlled. This design exhibits substantial potential for applications in terahertz detection, stealth technology, and related fields.

In summary, although research on 1D DS photonic crystals is gradually increasing, it has mainly focused on using DS as dielectric layers to form composite structures with other materials. In this paper, a symmetric 1D DS-defected photonic crystal structure is proposed. The transmission properties of this photonic crystal across multiple THz bands are investigated. The effects of different Fermi levels, Fermi velocities, degeneracy factors, angles of incidence, and material thickness on the transmission characteristics are analyzed in detail. This study not only enhances the understanding of the application of DS in photonic crystals but also provides new insights for the development of next-generation THz technology.

2. Theoretical model and formulations

To investigate the transport properties of 1D photonic crystals with DS defects, the following structure, $(AB)^N CDC(BA)^M$, has been designed. Where material A has a dielectric constant of $\varepsilon_A = 11.9$, material B has a dielectric constant of $\varepsilon_B = 3.9$, and material C has a dielectric constant of $\varepsilon_C = 2.5$, with thicknesses d_A, d_B, and d_C, respectively. D represents the DS-defected layer with a thickness of d_D.

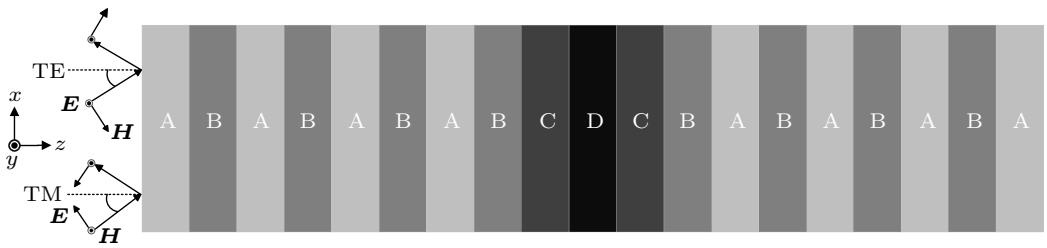


Fig. 1. Schematic structure of $(AB)^N CDC(BA)^M$ 1D photonic crystal containing a DS-defected layer, where M and N are periodic numbers, A, B, C are dielectric layers, and D is the DS.

When an electromagnetic wave is incident on a multilayer structure, it interacts with the material properties and geometric arrangement of each layer. The angle of incidence plays a crucial role in determining the wave's behavior as it propagates through the medium. For transverse electric polarized waves (TE), the electric field vector is oriented perpendicular to the plane of incidence, while the z-axis is defined as the direction of propagation. This configuration ensures that the magnetic field lies within the plane of incidence. TE polarization is particularly relevant for investigating wave interactions

in layered materials, such as thin films, metamaterials, or photonic crystals. The transfer matrix method is a mathematical technique used to correlate the electromagnetic field components within each layer of a structured medium. It is particularly effective for analyzing wave propagation through layered media. The propagation of light waves in a photonic crystal can be described by a total transfer matrix, which is obtained by multiplying the individual transfer matrices corresponding to each layer, including the DS layers. Characterization matrix of a single-layer medium is

$$M_j(\Delta z,\omega)=\begin{pmatrix}\cos(k_{jz}\Delta z) & \dfrac{\mathrm{i}}{q_{jz}}\sin(k_{jz}\Delta z)\\ \mathrm{i}q_{jz}\sin(k_{jz}\Delta z) & \cos(k_{jz}\Delta z)\end{pmatrix}, \tag{1}$$

where $k_{jz}=\omega/c\sqrt{\varepsilon_j}\cdot\sqrt{\mu_j}\cdot\sqrt{1-(\sin^2\theta/\varepsilon_j\mu_j)}$ represents the wave vector component along the z-axis in the j-th layer of the medium, and c denotes the speed of light in vacuum. In TE waves $q_{jz}=\sqrt{\varepsilon_j}/\sqrt{\mu_j}\sqrt{1-(\sin^2\theta/\varepsilon_j\mu_j)}$ and in TM waves $q_{jz}=\sqrt{\mu_j}/\sqrt{\varepsilon_j}\sqrt{1-(\sin^2\theta/\varepsilon_j\mu_j)}$. To simplify the calculations, the case of TE polarization is used in the following studies. So we can get the transfer matrix of the structure as

$$M_{\text{total}}=M_1M_2\cdots M_N, \tag{2}$$

the transmission coefficient can be expressed as

$$t=\frac{2\eta_1}{\eta_1(M_{11}+\eta_2M_{12})+M_{21}+\eta_2M_{22}}, \tag{3}$$

transmittance T reads

$$T=|t|^2, \tag{4}$$

where $\eta_1=\eta_2=\cos\theta$.

The dynamic conductivity can be derived using the Kubo formula under the random phase approximation

$$\mathrm{Re}\,\sigma(\Omega) = \frac{e^2}{\hbar}\frac{gk_{\mathrm{F}}}{24\pi}\Omega G(\Omega/2), \tag{5}$$

$$\mathrm{Im}\,\sigma(\Omega) = \frac{e^2}{\hbar}\frac{gk_{\mathrm{F}}}{24\pi^2}\left\{\frac{4}{\Omega}\left[1+\frac{\pi^2}{3}\left(\frac{T}{E_{\mathrm{f}}}\right)^2\right] +8\Omega\int_0^{\varepsilon_{\mathrm{c}}}\left[\frac{G(\varepsilon)-G(\Omega/2)}{\Omega^2-4\varepsilon^2}\right]\varepsilon\,\mathrm{d}\varepsilon\right\}, \tag{6}$$

where $G(E)=n(-E)-n(E)$ is the Fermi distribution function, g is the degeneracy factor, E_{f} is the Fermi level, $k_{\mathrm{F}}=E_{\mathrm{f}}/\hbar v_{\mathrm{F}}$ is the Fermi momentum, v_{F} is the Fermi velocity, $\Omega=\hbar\omega/E_{\mathrm{f}}$ is the normalized frequency, $\varepsilon_{\mathrm{c}}=E_{\mathrm{c}}/E_{\mathrm{f}}$, E_{c} is the cutoff energy, beyond which the Dirac spectrum is no longer linear, and e is the charge of the electron, from Eqs. (5) and (6) the conductivity is closely related to the material parameters, such as Fermi levels, Fermi velocities, and degeneracy factor.

Figures 2(a) and 2(b) illustrate the variations of the real and imaginary parts of the dynamic conductivity with normalized frequency at different Fermi levels, respectively. It can be observed that $\Omega=2$ serves as the critical point for the conductivity trend transition. For the real part, it does not exist when $\Omega<2$. Once the critical value is crossed, the real part undergoes a sudden jump and then gradually increases. For the imaginary part, when $\Omega<2$, it decreases gradually, reaching its minimum at $\Omega=2$, and then starts to increase beyond the critical value. As the Fermi level increases, the overall trend of conductivity change remains the same, but the magnitude of variation becomes more pronounced.

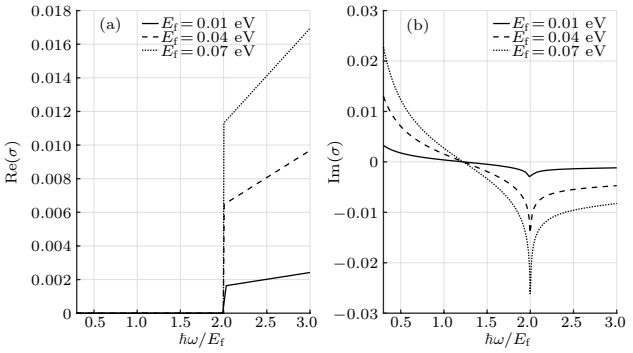


Fig. 2. (a) Real and (b) imaginary parts of the dynamic conductivity, σ, with normalized frequency $\Omega=\hbar\omega/E_{\mathrm{f}}$, at Fermi levels of 0.01 eV (solid line), 0.04 eV (dashed line), and 0.07 eV (dotted line), respectively, where $g=4$, $\varepsilon_{\mathrm{c}}=3$, $v_{\mathrm{F}}=10^6$ m/s.

The dynamic conductivity of the DS consists of interband and intraband conductivities, which can be expressed as[34]

$$\varepsilon=\varepsilon_\infty+\sigma/\omega\varepsilon_0, \tag{7}$$

$\varepsilon_\infty=13$ is the effective background permittivity, and ε_0 is the permittivity in vacuum.

Figure 3 presents the real and imaginary parts of the dielectric constant of DS at different Fermi levels. As shown in Fig. 3(a), the real part of the dielectric constant becomes negative within a certain frequency range for all three Fermi levels, indicating that DS exhibits metal-like properties in this range. As the frequency increases, the real part gradually rises from negative to positive at a certain critical frequency. After a slight increase to its peak value, it gradually stabilizes. Higher Fermi levels correspond to higher critical frequencies. As shown in Fig. 3(b), before reaching the critical frequency, the imaginary part of the dielectric constant remains closed to zero, indicating extremely low electromagnetic loss in DS. Beyond the critical frequency, the imaginary part increases and stabilizes, signifying a significant increase in electromagnetic loss in DS. The increasing of Fermi level only shifts the critical frequency at which the imaginary part appears but does not affect its magnitude. The dielectric constant of DS is highly sensitive to the Fermi level. With the increasing of the Fermi level, both the critical frequency of the real part and the

low-loss frequency range of the imaginary part expand significantly. Additionally, in Figs. 3(a) and 3(b), when the real part of the dielectric constant peak achieves the maximum value, the imaginary part of the dielectric constant begins to emerge at the same frequency.

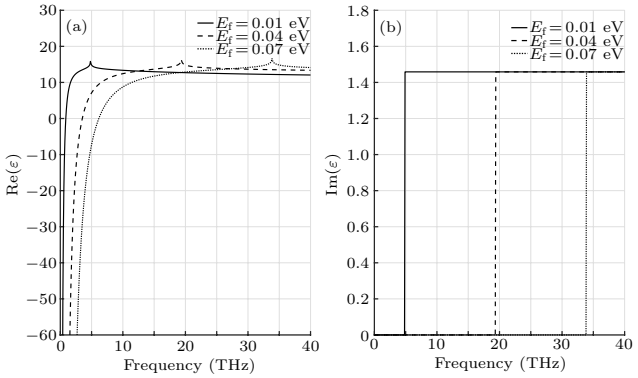


Fig. 3. (a) Real and (b) imaginary parts of the Dirac semimetal permittivity for Fermi levels of 0.01 eV (solid line), 0.04 eV (dashed line), and 0.07 eV (dotted line), respectively, where $g = 4$, $\varepsilon_c = 3$, $v_F = 10^6$ m/s, $\varepsilon_\infty = 13$.

3. Results and discussion

In this paper, the transmission properties of 1D DS photonic crystals of structure $(AB)^N CDC(BA)^M$ are investigated in the THz band. The parameters chosen for the calculations are as follows: $N = M = 4$, $d_A = 4$ μm, $d_B = 8$ μm, $d_C = 1$ μm, $d_D = 0.5$ μm, $\varepsilon_c = 3$, $\mu_A = \mu_B = \mu_C = 1$, and $\mu_D = 3$.

3.1. Transmission characteristics at different Fermi levels

In this section, the transmission properties of this 1D photonic crystal structure at different Fermi levels are discussed. Based on the previous experimental works,[35–37] the application of an external voltage can precisely tune the position of the Fermi level by influencing the electric field within the DS materials. The change of the electric field can alter the carrier concentration, which in turn affects the electron distribution and the band structure, especially the position of the Fermi level.

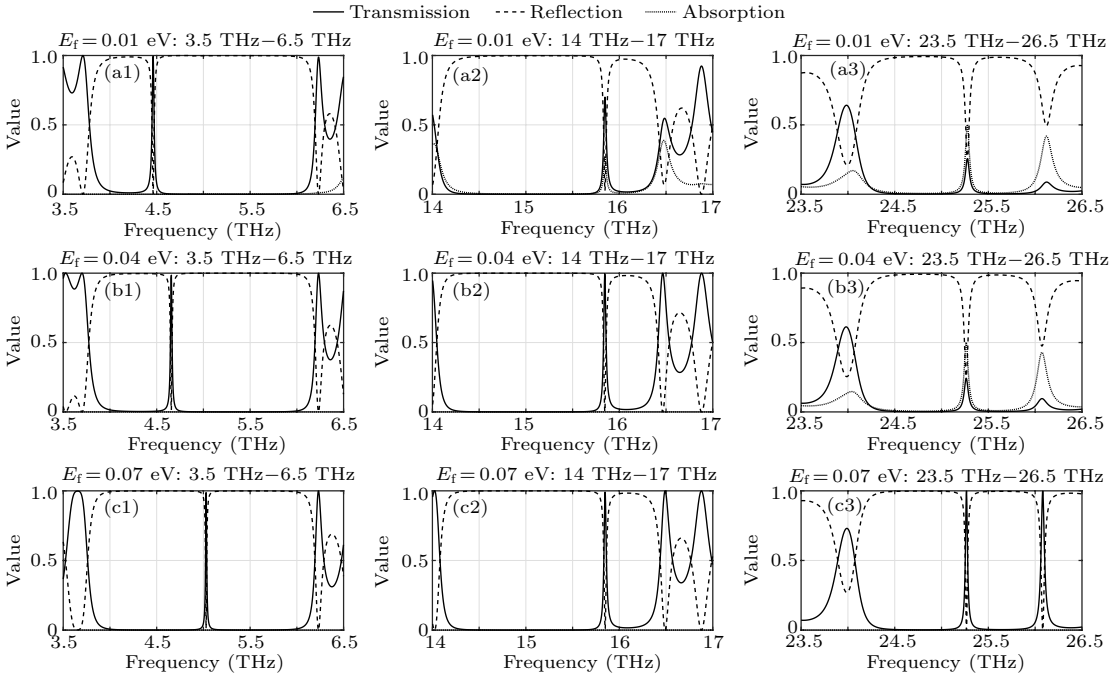


Fig. 4. Analysis of the transmission characteristic curves of structure $(AB)^N CDC(BA)^M$ at Fermi levels of (a) 0.01 eV, (b) 0.04 eV, and (c) 0.07 eV using the transmission matrix method, where $v_F = 10^6$ m/s, $g = 4$, $\varepsilon_c = 3$, $\varepsilon_\infty = 13$.

As shown in Fig. 4, the introduction of DS defects produces sharp transmission peaks in the photonic forbidden band. With the gradual increase of the Fermi level, a nearly complete bandgap structure appears in the frequency range of 3.5 THz–6 THz in Figs. 4(a1), 4(b1), and 4(c1), with a transmission peaks induced by the defect structure of the DS. In this range, no significant light absorption occurs, indicating that the light wave undergoes resonant transmission within the photonic crystal. The position and intensity of the transmission peaks are strongly influenced by the Fermi level of the DS. As the Fermi level increases, the transmission peaks shift to higher frequencies. Within the frequency range of 14 THz–17 THz, absorption peaks emerge at a Fermi level of 0.01 eV, while near-complete photonic bandgaps are observed at Fermi levels of 0.04 eV and 0.07 eV. In Fig. 4(a2), at a Fermi level of 0.01 eV, the height of the transmission peak significantly decreases, accompanied by the emergence of an absorption peak. In Figs. 4(b2) and 4(c2), a complete bandgap structure reappears, along with absorption-free transmission peaks. Similarly, In the 23.5 THz–26.5 THz band, absorption occurs at Fermi levels of 0.01 eV and 0.04 eV. Almost complete bandgap structure occurs at 0.07 eV. In Figs. 4(a3), 4(b3), and 4(c3), when the Fermi level is 0.01 eV and 0.04 eV, the DS exhibits metal-like properties, accompanied by absorption

peaks. When the Fermi level increases to 0.07 eV, the imaginary part of the DS dielectric constant disappears, causing the semimetal to behave as a non-absorbing medium in this frequency band, leading to the appearance of high transmission peaks. The change in transmission properties is closely related to the variation in the dielectric constant shown in Fig. 3. As the Fermi level increases, the real part of the dielectric constant decreases at the same frequency, while the critical frequency for the emergence of the imaginary part shifts to higher frequencies, causing the DS to transition from a dielectric to a metallic material. This transformation results in the reappearance of high transmission peaks at higher frequency ranges and a reduction in light absorption.

Thus, it is evident that changes in the Fermi level significantly impact the transmission properties of photonic crystals.

3.2. Transmission characteristics at different Fermi velocities

The Fermi velocity is a physical quantity that describes the speed of electron propagation near the Fermi surface and is closely related to the electrodynamic properties of materials. The Fermi velocity-dependent dielectric response serves as a critical mechanism for tailoring photonic bandgaps and electromagnetic mode distributions in photonic crystals, enabling active control of light–matter interactions. The experimental methods for controlling the Fermi velocity include tuning the chemical potential, chemical doping and alloying, symmetry breaking (e.g., breaking $C4$ symmetry), and surface state engineering.[38,39] By modulating the Fermi velocity, the propagation properties of electromagnetic waves in DS-based photonic crystals can be effectively controlled.

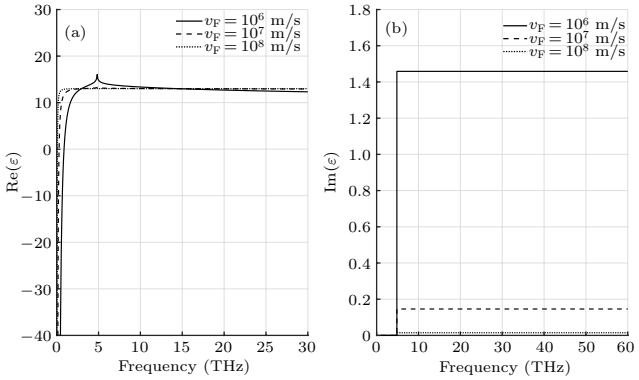


Fig. 5. (a) Real and (b) imaginary parts of the DS dielectric constant when the Fermi velocities are $v_F = 10^6$ m/s (solid line), $v_F = 10^7$ m/s (dashed line), and $v_F = 10^8$ m/s (dotted line) respectively, where $E_f = 0.01$ eV, $g = 4$, $\varepsilon_c = 3$, $\varepsilon_\infty = 13$.

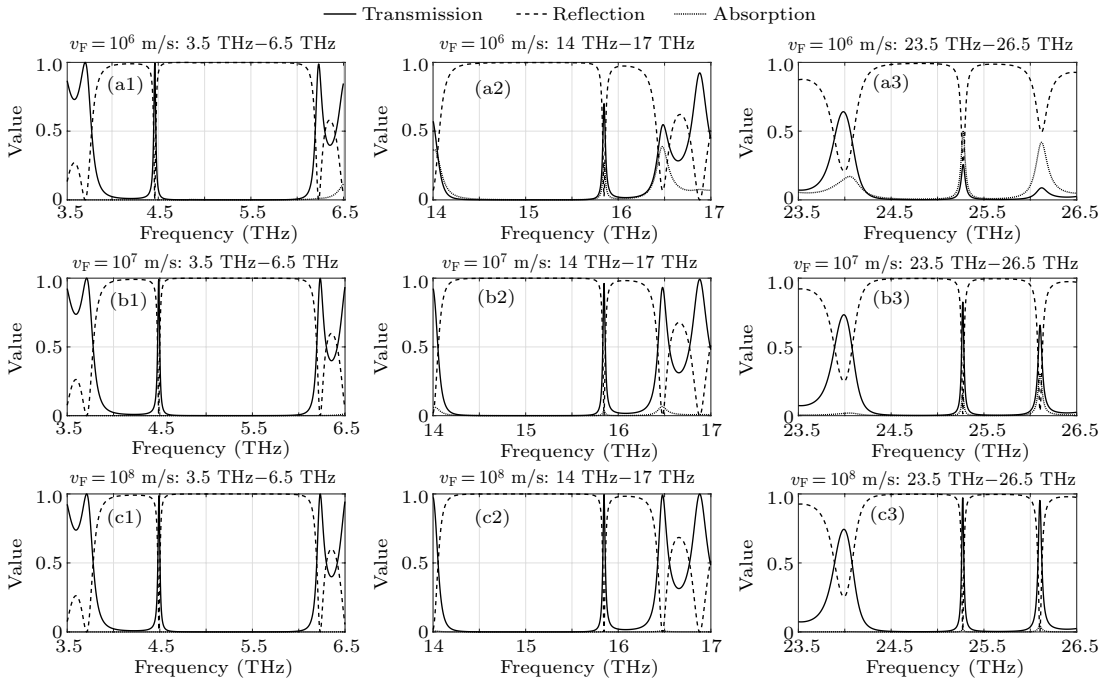


Fig. 6. Transmission characteristics for Fermi velocities (a) $v_F = 10^6$ m/s, (b) $v_F = 10^7$ m/s, and (c) $v_F = 10^8$ m/s respectively, where $E_f = 0.01$ eV, $g = 4$, $\varepsilon_c = 3$, $\varepsilon_\infty = 13$.

The Fermi velocity is shown in Eqs. (5) and (6), and the Fermi momentum directly affects the dielectric constant of the material. The real part of the dielectric constant changes with different Fermi velocities as shown in Fig. 5(a). It can be seen that the real part of the dielectric constant achieves the highest value first with the higher Fermi velocity and then gradually stabilizes. The variation of the imaginary part is shown in Fig. 5(b), where the variation in Fermi velocity does not affect the critical value of the appearance of the imaginary part. However, after crossing the critical value, the larger the Fermi velocity is, the smaller the imaginary part of the dielectric constant can achieve. The transmission characteristics at different Fermi velocities are shown in Fig. 6. In Fig. 6(a1), a complete photonic bandgap and a full transmission defect peak are formed in the frequency range of 3.5 THz–6 THz; in Figs. 6(b1) and 6(c1), the increase in Fermi velocity has no effect on the transmission characteristics in this frequency band. In Figs. 6(a2) and 6(b2), there appears the absorp-

tion of the defect peak in the frequency range of 14 THz–16.5 THz. However, the increasing of Fermi velocity makes the transmission defect peak gradually get stronger until it reaches the maximum in panel (c2), forming a complete defect peak. In the 23.5 THz–26.5 THz frequency band, the absorption of the defect peak is larger than the previous two photonic bandgap, while the peak intensity of the transmission gradually increases, and the absorption rate gradually decreases with the Fermi velocity as shown in Figs. 6(a3) and 6(b3). This corresponds to the change in the imaginary part of the dielectric constant as shown in Figs. 5(a) and 5(b). After crossing the critical value, the larger the Fermi velocity is, the smaller the imaginary part of the dielectric constant becomes, which can lead to a reduction in the absorption rate of light.

3.3. Transmission characteristics at different degeneracy factors (g)

The degeneracy factor is a key parameter in the Dirac semimetal system and refers to the number of degenerate states in the energy band structure. Based on experimental results,[40] Dirac semimetals exhibit the following typical values of degeneracy factors: $g = 40$ for AlCuFe quasicrystals, $g = 24$ for systems such as Eu_2IrO_7 or the TaAs family, and $g = 4$ for materials including Na_3Bi and Cd_3As_2. An increase in the degeneracy factor g enhances both the conductivity amplitude and the imaginary component of the dielectric function across the frequency range, thereby accentuating the metallic character of the DS.

In this subsection, we discuss the effect of different degeneracy factors on transmission characteristics for $E_f = 0.04$ eV, $v_F = 10^6$ m/s. As shown in Fig. 8, within the range of 3.5 THz–6.5 THz, the transmission peak shifts toward higher frequencies with increasing g values while maintaining invariant intensity, jointly forming a complete photonic bandgap with the reflectivity. This phenomenon corresponds to the variation of the real part of the dielectric constant in Fig. 7(a). Meanwhile, the imaginary part has not yet reached the critical value, so no significant absorption properties are observed in this band. In the frequency range of 14 THz–17 THz as shown in Figs. 8(a2), 8(b2), and 8(c2), the transmission characteristics do not change significantly with increasing g. However, in the range of 23.5 THz–26.5 THz, the bandgap structure gradually disappears, the transmission decreases, and absorption phenomena appear in multiple frequency bands, as shown in Figs. 8(a3), 8(b3), and 8(c3). The DS with different g values exhibits significant differences in electromagnetic response. By adjusting the degree of degeneracy (e.g., through doping or selecting materials with different crystal symmetries), it can be achieved to switch the status of the DS system between metallic and dielectric responses, further optimizing their applications in photonics and plasmonic devices.

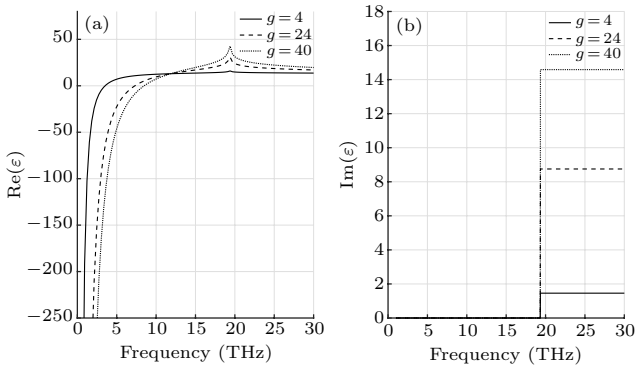


Fig. 7. (a) Real and (b) imaginary parts of the DS dielectric constant when the degeneracy factors are $g = 4$ (solid), 24 (dashed), and 40 (dotted) lines, where $E_f = 0.04$ eV, $v_F = 10^6$ m/s.

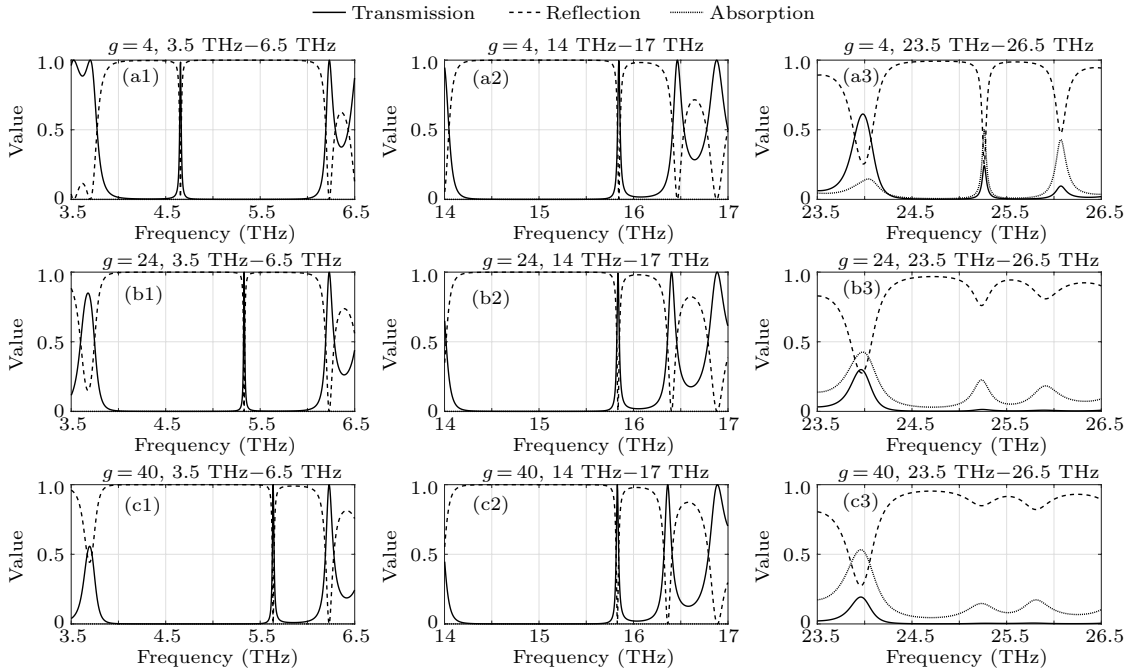


Fig. 8. Transmission characteristics for different degeneracy factors $g = 4$ (a), 24 (b), 40 (c), where $E_f = 0.04$ eV, $v_F = 10^6$ m/s.

3.4. Transmittance at different angles of incidence

The effect of incident angle on the transmission property is illustrated as shown in Fig. 9. As the incident angle increases, the transmittance property exhibits a nonlinear variation in this range, and the overall transmission peaks shift toward higher frequencies. In Fig. 9(a), the defect peak remains around 4.5 THz, and its intensity is slightly affected by the incident angle. In the frequency range of 14 THz–17 THz, the defect peak shifts toward higher frequencies, and its peak intensity decreases from 0.7 to 0.6 as the incident angle increases from 0° to 45°, with the transmission peak shifting from 15.8 THz to 16.7 THz as shown in Fig. 9(b). In Fig. 9(c), the intensity and shift of the defect peak are more significantly affected by the incident angle, and the defect peak disappears in this band when the angle increases to 43°.

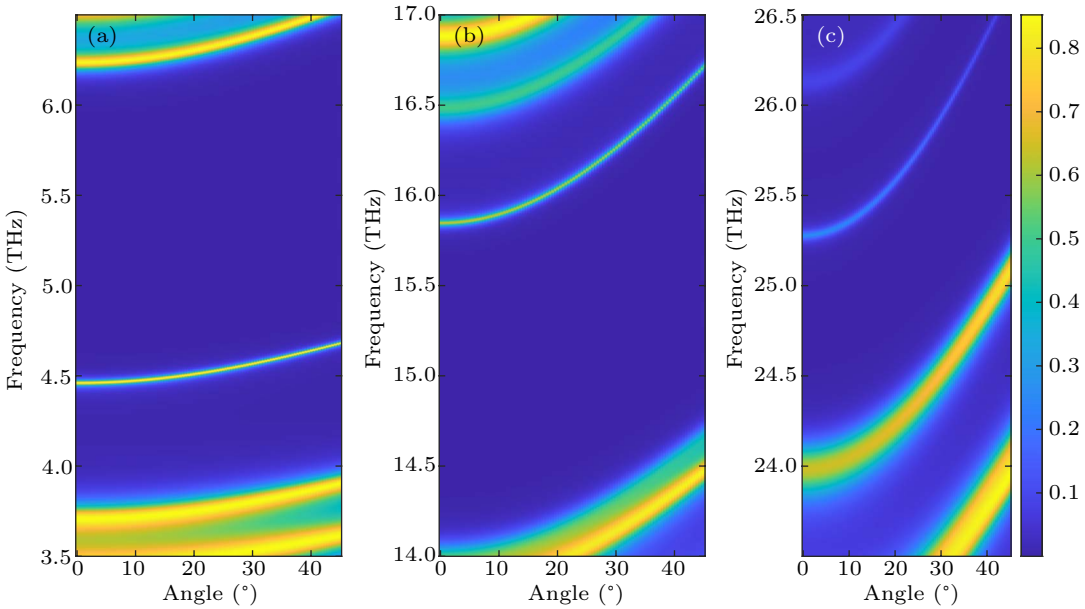


Fig. 9. Transmission peaks *versus* angles of incidence are presented for the frequency ranges (a) 3.5 THz–6.5 THz, (b) 14 THz–17 THz, and (c) 23.5 THz–26.5 THz, where $E_f = 0.01$ eV, $v_F = 10^6$ m/s, $g = 4$.

3.5. Transmittance at different defect layer thicknesses

In addition to the influence of the parameters of the DS itself, the thickness of the defect layer also plays a crucial role in propagation characteristics. This section discusses the effect of defect mode thickness variation on transmission characteristics when the Fermi level is fixed and $E_f = 0.04$ eV, $v_F = 10^6$ m/s, $g = 4$. In Fig. 10(a), as the thickness of the defect layer increases from 0.5 μm to 1.5 μm, the transmission peak gradually shifts to the low-frequency direction. Similarly, in Fig. 10(b), the transmission peak exhibits a more pronounced low-frequency shift, moving from 15.8 THz to 14.7 THz.

The formula of the position of the frequency of the defected mode can be derived as $f = \frac{mc}{2n_d} \times \frac{1}{d}$ yielding $f \propto \frac{1}{d}$, from which it can be seen that the resonance frequency is inversely proportional to the thickness of the defect layer.[41] Therefore, as shown in Fig. 10, the defect mode shifts toward lower frequencies (longer wavelengths) with increasing defect layer thickness. Meanwhile, the intensity of the defect peak remains unchanged across the frequency ranges.[42] It is attributed to the fact that the DS exhibits dielectric rather than metallic characteristics within this frequency range.

These changes show that adjusting the DS thickness affects the transmission spectrum and allows tuning of the defect mode over a wide frequency range, improving the structure's electromagnetic properties.

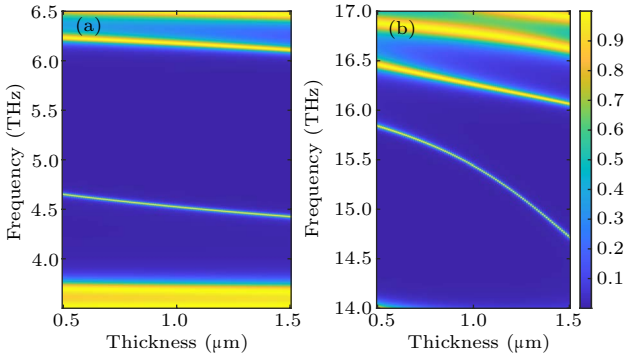


Fig. 10. Transmission peak evolution for DS thicknesses of 0.5 μm–1.5 μm: (a) 3.5 THz–6.5 THz and (b) 14 THz–17 THz, where $E_f = 0.04$ eV, $v_F = 10^6$ m/s, $g = 4$.

4. Conclusions

In this study, the transmission properties of 1D photonic crystals with DS defects are investigated using the transfer matrix method, and the effects of various parameter variations on the transmission behavior are analyzed. An increasing in the Fermi level raises the critical threshold for the transition of DS from a dielectric to a metallic state. When the Fermi level is

0.01 eV, a complete photonic bandgap with defect modes appears in the low-THz frequency range, while absorption occurs in the mid- and high-THz frequency ranges. At a Fermi level of 0.04 eV, defect-mode photonic bandgaps form in the low and mid-THz frequency bands, with absorption still present at high frequencies. A Fermi level of 0.07 eV results in complete defect-mode bandgaps across the low, mid, and high-THz frequency regions. The Fermi velocity and the degeneracy factor influence the magnitude of the imaginary part of the DS dielectric constant. The Fermi velocity is inversely proportional to the metallic properties of the material; as it increases, absorption in the mid- and high-THz frequency bands weakens, resulting in enhancing of the transmission peak. Conversely, the degeneracy factor is directly proportional to the metallic nature, and its variation causes the defect peak in the low-THz frequency region to shift from 4.6 THz to 5.6 THz. It does not affect the transmission in the mid-THz frequency range but disrupts the bandgap structure in the high-THz frequency region. In addition, increasing the thickness of the defect layer significantly shifts the defect mode toward lower frequencies. Under oblique incidence, defect modes shift toward higher frequencies due to the influence of the incident angle. Appropriately tuning structural parameters can optimize transmission performance and enable optimal design in practical applications. These results provide a theoretical foundation for optimizing the design parameters of photonic crystals. The unique electronic and optical properties of DS offer great potential for applications in 1D photonic crystal devices.

References

[1] Yordanov P, Priessnitz T, Kim M, Cristiani G, Logvenov G, Keimer B and Kaiser S 2023 *Adv. Mater.* **35** 2305622
[2] Bradley S and Zhang X C 2002 *Nat. Mater.* **1** 26
[3] Nagel M, Haring Bolivar P, Brucherseifer M, Kurz H, Boßerhoff A and Büttner R 2002 *Appl. Phys. Lett.* **80** 154
[4] Dekorsy T, Auer H, Waschke C, Bakker H J, Roskos H G, Kurz H, Wagner V and Grosse P 1995 *Phys. Rev. Lett.* **74** 738
[5] Yablonovitch E 1987 *Phys. Rev. Lett.* **58** 2059
[6] John S 1987 *Phys. Rev. Lett.* **58** 2486
[7] Zhang H F, Liu S B, Kong X K, Bian B R and Zhao H C 2012 *Opt. Commun.* **285** 5235
[8] Qi D, Wang X and Cheng Y Z 2016 *Opt. Mater.* **62** 52
[9] Liu B, Shi J, Zhang J K, Li Z G, Chen Z S and Deng X S 2021 *Opt. Mater.* **111** 110689
[10] Yang J Y, Ghimire I, Wu P C, Gurung S, Arndt C, Tsai D P and Lee H W H 2019 *Nano Photon.* **8** 443
[11] Huang H L, Xiao N, Kariyado T, Amemiya T and Hu X 2023 *Opt. Express* **31** 27006
[12] Jamshidi-Ghaleh K and Ebrahimpour Z 2013 *Eur. Phys. J. D* **67** 27
[13] Novoselov K S, Geim A K, Morozov S V, Jiang D, Zhang Y, Dubonos S V, Grigorieva I V and Firsov A A 2005 *Nature* **438** 197
[14] Jahani D, Alidoust Ghatar A and Abaspour L 2020 *Mater. Sci. Eng. B* **261** 114626
[15] Sattarian H, Shojaei S and Darabi E 2017 *Opt. Quantum Electron.* **49** 319
[16] Schwierz F 2010 *Nat. Nano Technol.* **5** 487
[17] Liu J T, Liu N H, Li J, Li X J and Huang J H 2012 *Appl. Phys. Lett.* **101** 052104
[18] Liu Z K, Jiang J, Zhou B, Wang Z J, Zhang Y, Weng H M, Prabhakaran D, Hashimoto M, Han P, Dudin P, Kim T K, Hoesch M, Fang Z, Dai X, Shen Z X, Feng D L, Hussain Z and Chen Y 2014 *Nat. Mater.* **13** 677
[19] Wang L X, Li C Z, Yu D P and Liao Z M 2016 *Nat. Commun.* **7** 10769
[20] Liu C X, Zhang H J, Yan B H, Qi X, Frauenheim T, Dai X, Fang Z and Zhang S C 2010 *Phys. Rev. B* **81** 041307
[21] Xu B, Dai Y M, Zhao L J, Wang K, Yang R, Zhang W, Liu J Y, Xiao H, Chen G F, Taylor A J, Yarotski D A, Prasankumar R P and Qiu X G 2016 *Phys. Rev. B* **93** 121110
[22] Liang T, Gibson Q, Ali M N, Liu M H, Cava R J and Ong N P 2014 *Nat. Mater.* **14** 280
[23] Young S M, Zaheer S, Teo J C Y, Kane C L, Mele E J and Rappe A M 2012 *Phys. Rev. Lett.* **108** 140405
[24] Xiong J L, Kushwaha S, Liang T, Krizan J W, Hirschberger M, Wang W, Cava R J and Ong N P 2015 *Science* **350** 413
[25] Neupane M, Xu S, Sankar R, Alidoust N, Bian G, Liu C, Belopolski I, Chang T R, Jeng H T, Lin H, Bansil A, Chou F C and Hasan M Z 2014 *Nat. Commun.* **5** 3786
[26] Cao J X, Liang S F, Zhang C, Liu Y W, Huang J W, Zhao J H, Chen Z G, Wang Z J, Wang Q S, Zhao J, Li S Y, Dai X, Zou J, Xia Z C, Li L and Xiu F 2015 *Nat. Commun.* **6** 7779
[27] Zhao Y K, Zhang Y P, Guo X H, Liu M D, Chen H, Liu S D and Zhang H Y 2017 *J. Appl. Phys.* **122** 223108
[28] Wang Q, Wang X L, Zhang L W, Wang Y Q, Qiao W T, Han X, Cai X L and Yu W Y 2018 *Appl. Opt.* **58** 94
[29] You Y and Da H X 2023 *J. Opt. Soc. Am. B* **40** 360
[30] Wang T L, Zhang H Y, Zhang Y, Zhang Y P and Bai X Z 2020 *Opt. Express* **28** 17434
[31] Meng H Y, Shang X J, Xue X X, Tang K Z, Xia S X, Zhai X, Liu Z R, Chen J H, Li H J and Wang L L 2019 *Opt. Express* **27** 31062
[32] Wang L, Han L, Guo W L, Zhang L B, Yao C Y, Chen Z Q Z, Chen Y L, Guo C, Zhang K X, Kuo C N, Lue C S, Politano A, Xing H Z, Jiang M J, Yu X B, Chen X S and Lü W 2022 *Light Sci. Appl.* **11** 53
[33] Li Y, Zhai X, Xia S X, Li H J and Wang L L 2020 *J. Phys. D: Appl. Phys.* **53** 205106
[34] Chen H, Zhang H Y, Liu M D, Zhao Y K, Guo X H and Zhang Y P 2017 *Opt. Mater. Express* **7** 3397
[35] Zheng Q W, Lü W, Xu J, Ye Y, Zhao X Z and Jiang L Y 2023 *Chin. Phys. B* **32** 074208
[36] Yu Y J, Zhao Y, Ryu S M, Brus L E, Kim K S and Kim P 2009 *Nano Lett.* **9** 3430
[37] Wang S, Lin B C, Zheng W Z, Yu D and Liao Z M 2018 *Phys. Rev. Lett.* **120** 257701
[38] Moll P J W, Nair N, Helm T, Potter A C, Kimchi I, Vishwanath A and Analytis J 2016 *Nature* **535** 266
[39] Liu Z K, Zhou B, Zhang Y, Wang Z J, Weng H M, Prabhakaran D, Hashimoto M, Shen Z X, Fang Z, Dai X, Hussain Z and Chen Y 2014 *Science* **343** 864
[40] Kotov O V and Lozovik Y E 2016 *Phys. Rev. B* **93** 235417
[41] Wu F, Liu T T, Chen M Y and Xiao S Y 2022 *Opt. Express* **30** 33911
[42] Lang Y P, Liu Q G, Wang Q, Zhou X and Jia G Y 2023 *Chin. Phys. B* **32** 017802